applied sciences

MDPI

Article

Simulation of Vapor-Liquid Separation in the Orifice-Baffle Header under Various Operating Conditions

Kunteng Huang [1], Jianyong Chen [1,2,*], Ying Chen [1,2], Xianglong Luo [1,2], Yingzong Liang [1,2], Jiacheng He [1,2] and Zhi Yang [1,2]

[1] School of Material and Energy, Guangdong University of Technology, Guangzhou 510006, China
[2] Guangdong Provincial Key Laboratory of Functional Soft Condensed Matter, Guangzhou 510006, China
* Correspondence: jianyong@gdut.edu.cn

Abstract: Vapor-liquid separation during condensation enables the enhancement of heat transfer coefficient and reduction in pressure drop simultaneously. The vapor-liquid separator is vital to the performance of such a liquid-separation condenser (LSC). It should fulfill the functions of allowing the condensate to drain away as much as possible from the separator and leaving only vapor to continue condensing afterwards. However, due to the intensive interactions between the liquid and vapor, it is really hard to achieve perfect vapor-liquid separation, adding new uncertainties to the maldistributions in the branch outlets of a parallel condenser. To discover more insights of the flow conditions in the header and phase distributions, the characteristics of the orifice-baffle header are studied by using CFD and the mechanistic model for the droplet analysis is established by means of force balance in this paper. A parametrical analysis is carried out to discover the effects of operating conditions. It is found that the maximum vapor-liquid separation efficiency (η) is 51.94% as the inlet mass flow rate ($\dot{m}_{in}$) is 12 g/s. The vapor leakage from the orifice because of the liquid impact is one of the main reasons that deteriorate the vapor-liquid separation performance. Moreover, the vortex in the header increases the local mass flux, thereafter decreasing the droplet diameter. With the increasing of $\dot{m}_{in}$, the dominant force of the droplet in the vertical direction switches from F_G to F_{D2}.

Keywords: condenser; vapor-liquid separation; simulation; separation efficiency

Citation: Huang, K.; Chen, J.; Chen, Y.; Luo, X.; Liang, Y.; He, J.; Yang, Z. Simulation of Vapor-Liquid Separation in the Orifice-Baffle Header under Various Operating Conditions. *Appl. Sci.* **2022**, *12*, 7971. https://doi.org/10.3390/app12167971

Academic Editor: Xiaohong Han

Received: 21 July 2022
Accepted: 5 August 2022
Published: 9 August 2022

1. Introduction

The vapor phase is generally converted into the liquid phase during condensation. The condensate accumulates on the heat transfer surface and the liquid film becomes thicker and thicker, leading to the increasing of thermal resistance and flow resistance. Peng et al. [1] proposed the concept of "liquid-separation condensation" to enhance the condenser performance. The configuration of a liquid-separation condenser (LSC) is shown in Figure 1a. The condensate can be promptly removed by the vapor-liquid separator in the headers. To deal with the alleviated mass flow rate due to the liquid drainage, the flow area should be shrunk accordingly to keep the pace of variations in mass flux. In this way, the thickness of the liquid film is largely reduced and the vapor quality is significantly improved, which finally enhances the heat transfer coefficient (HTC), as shown in Figure 1b.

Researchers have verified the superiorities of LSC. Hua [3] theoretically found that HTC of LSC can be 34.6% higher and the pressure drop can be 74.4% lower than the conventional condenser. Zhong et al. [4] experimentally confirmed that when the mass flux is higher than 590 km/(m^2·s), LSC has a higher heat transfer coefficient and 30.5–52.6% lower pressure drop, simultaneously. They further pinpointed that LSC has superior comprehensive performance in terms of penalty factor and minimum entropy generation number [5]. Li et al. [6] discovered that the condenser inserted with a T-junction unit can improve the heat transfer capacity by approximately 5.1%. At the level of the thermal systems, LSC also exhibits its advances in air conditioning systems, heat pump, and organic Rankine

cycle (ORC). Chen et al. [7] found that the Energy Efficiency Ratio (EER) at cooling mode and Coefficient of Performance (COP) at heating mode in an air conditioning with LSC are 9.8% and 7.3% higher than these in baseline system, respectively. They further pointed out that using LSC can reduce avoidable exergy destruction of the compressor by 45.5% [8]. Li et al. [6] found that the refrigeration system with LSC results in a higher COP by 6.6% compared to a conventional condenser. Chen et al. [9] revealed that the heat pump with LSC has a higher COP and lower power consumption. Lu et al. [10] concluded that the ORC with LSC achieves a 21.43% lower average electricity production cost than conventional ORC. In short, liquid-separation condensation is a promising technology that enables the improvement of both the condenser performance and thermal system efficiency.

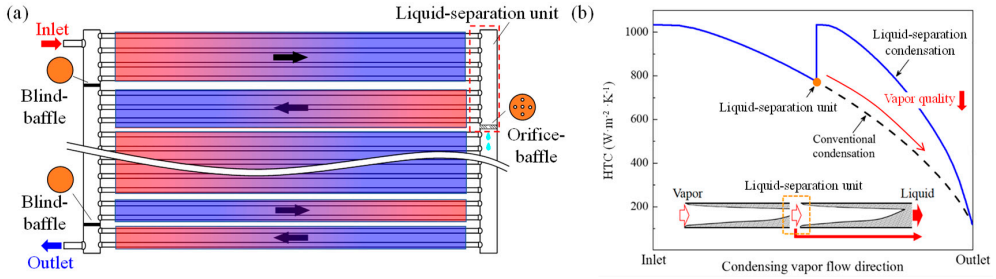

Figure 1. (**a**) Scheme of LSC; (**b**) HTC enhancement in LSC, modified from [2].

As one of the essential parameters, the vapor quality (x) largely determines HTC during condensation. The higher the vapor quality is, the higher the HTC becomes. In principle, for a superior HTC in LSC, it is preferable to have a high vapor quality that is close to one after the vapor-liquid separation. Therefore, the performance of the liquid-separation unit that dominates the redistributions of vapor quality and mass flow rate is vital to LSC. More attention should be paid to the liquid-separation unit.

Up to now, only two kinds, namely the T-junction header and the orifice-baffle header, are extensively employed in LSC.

LSC with a T-junction header is based on the differential inertia force of the liquid and vapor. It was proposed by Oh et al. [11]. Li et al. carried out a comprehensive study on this T-junction header, including a visualization experiment [12], theoretical model [13] and the CFD model [14]. They found that the liquid drainage ratio (F_L) can be 100% at low inlet mass flux, and it reduces with the increasing of the inlet mass flux or inlet quality. However, in the T-junction header, the liquid and vapor can only be separated one, which limited the improvement of HTC in LSC.

Alternatively, the vapor-liquid separation in the orifice-baffle header is on the basis of gravitation force. As shown in Figure 1, the two-phase flow from the branch inlets enters into the header where the vapor-liquid separation occurs on the orifice-baffle due to their distinct physical properties and the pressure difference across the orifices. Ideally, the liquid is accumulated on the orifice-baffle and drained out from the orifices, whereas the vapor flows out via the branch outlets. Hence, the phase separation is achieved. However, in practice, due to the intensive interactions between liquid and vapor, incomplete vapor-liquid separation occurs in the liquid-separation unit, thus limiting the potential release of liquid-separation condensation. Mo et al. [15] pointed out that in the orifice-baffle header of LSC, the vapor-liquid separation efficiencies of annular flow and slug flow at the inlet are 45% and 80%, respectively. Li et al. [16] established a numerical simulation model of the orifice-baffle header based on the Volume of Fluid (VOF) method. The results showed that when the diameter of the orifice is larger than 2 mm, the liquid drainage by the orifice is almost the same, and the vapor leakage rate of the orifice increases as well. The available studies on the orifice-baffle header have been simplified as one branch inlet and one branch outlet as well as only a single orifice in the center of the baffle. However, the branches and the orifices are multiple in the actual LSC [7]. Furthermore, the mass flow rate in the header is 2–5 g/s in Li et al. [16], which is substantially differentiated from that in LSC. The

interactions between the liquid and vapor are more intensive in LSC and there exists fluid maldistribution in multiple branches. In short, the vapor-liquid separation performance and the flow characteristic in the orifice-baffle header with multiple branches and orifices under various inlet operating conditions are quite different from the existing findings. Mechanics of vapor-liquid separation and flow maldistribution in the branch are still to be unveiled, and this is in great need of further exploration.

In this paper, a numerical simulation model for an orifice-baffle header with multiple branches and orifices is established and validated. The vapor-liquid separation features and the flow characteristics at various operating conditions are analyzed. This paper is of great importance to reveal the mechanisms of vapor-liquid separation and flow maldistribution.

2. Model Description

2.1. Computational Domain and Boundary Condition

Based on the previous LSC structure [17], the branch parameters of the orifice-baffle header are shown in Figure 2. The liquid-separation unit consists of four branch inlets and three branch outlets, namely I_1, I_2, I_3, I_4, B_1, B_2, and B_3 from top to bottom. Furthermore, the orifice is not assigned on the right side of the baffle to avoid the direct liquid impact. The boundary condition at the inlets and outlets are set as velocity inlet and pressure outlet, respectively. The velocity of each phase is calculated using the void fraction model proposed by EI Hajal et al. [18] and compiled by a user-defined function (UDF). The pressure difference between the branch outlet P_B and the orifice P_O approximately equals to the pressure drop in the next two paths of the LSC [17].

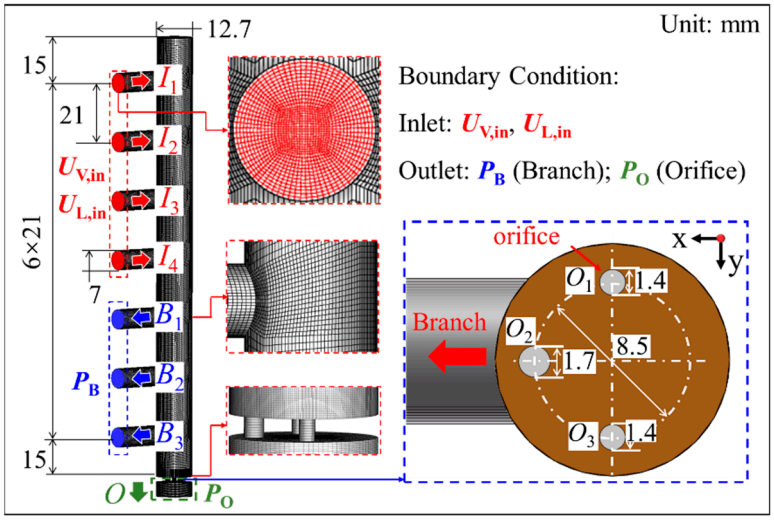

Figure 2. Scheme of the header and the boundary conditions.

2.2. Methematical Method

In this paper, the volume of fluid (VOF) multiphase model is used to simulate the two-phase flow owing to its special geo-reconstruction interpolation. Moreover, due to the intense interaction between liquid and vapor, the RNG k-ε turbulence model is also used. The Standard Wall Function is chosen to simulate the near-wall flow. The following assumptions are made for the simulation: (1) the fluid properties are constants. (2) two-phase fluid flows in the header are adiabatic and the mass transfer between vapor-liquid interface is not considered. The governing equation is shown in Table 1.

Table 1. Governing equations.

Parameters	Equations	
Volume Fraction	$\frac{\partial}{\partial t}(\alpha_q \rho_q) + \nabla\left(\alpha_q \rho_q \vec{u_q}\right) = 0$	(1)
	$\alpha_L + \alpha_V = 1$	(2)
Momentum	$\frac{\partial}{\partial t}\left(\rho \vec{u}\right) + \nabla \cdot \left(\rho \vec{u}\vec{u}\right) = -\nabla p + \nabla \cdot \left[\mu\left(\nabla \vec{u} + \nabla \vec{u}^{\mathrm{T}}\right)\right] + \rho \vec{g} + \vec{F}\sigma$	(3)
Properties	$\rho = \alpha_L \rho_L + \alpha_V \rho_V$	(4)
	$\mu = \alpha_L \mu_L + \alpha_V \mu_V$	(5)
Turbulence kinetic k	$\frac{\partial}{\partial t}(\rho k) + \nabla \cdot \left(\rho \vec{u} k\right) = \nabla \cdot \left[\left(\mu + \frac{\mu_t}{\sigma_k}\right)\nabla k\right] + G_k - \rho\varepsilon$	(6)
Turbulence kinetic dissipation ε	$\frac{\partial}{\partial t}(\rho\varepsilon) + \nabla \cdot \left(\rho \vec{u} \varepsilon\right) = \nabla \cdot \left[\left(\mu + \frac{\mu_t}{\sigma_\varepsilon}\right)\nabla\varepsilon\right] + C_{1\varepsilon}\frac{\varepsilon}{k}(G_k) - C_{2\varepsilon}\rho\frac{\varepsilon^2}{k}$	(7)
Generation of turbulent kinetic energy G_k	$G_k = \frac{\mu_t\left(\nabla u + \nabla u^{\mathrm{T}}\right)}{\nabla u}$	(8)
Eddy viscosity μ_t	$\mu_t = \rho C_\mu \frac{k^2}{\varepsilon}$	(9)

A segregated solver is employed for the transient-state process. The time step is set as 10^{-5} s. The governing equations are discretized by the Finite Volume Method (FVM). Furthermore, the residuals through every time step iterations are all lower than 10^{-4}. The discrete scheme and the under-relaxation factor as well as other details are found in our previous research [16].

2.3. Mesh-Sensitive Test and Model Validation

The geometry of the header is discrete by the hexahedral mesh (Figure 2) and the first layer of the mesh is set in the sub-layer region, in which y+ is larger than 11.225. Moreover, four sets of cases with different mesh numbers are simulated for the mesh-sensitive test. Figure 3a shows that when the mesh number is more than 2.03 million, the liquid drainage rate by the orifice ($\dot{m}_{L,O}$) changes insignificantly. Hence, to balance the calculation consumption and the accuracy of the numerical model, the mesh number of 2.03 million is selected, in which the minimum orthogonal quality, the maximum ortho skew and the aspect ratio are 0.54, 0.43 and 2.53, respectively.

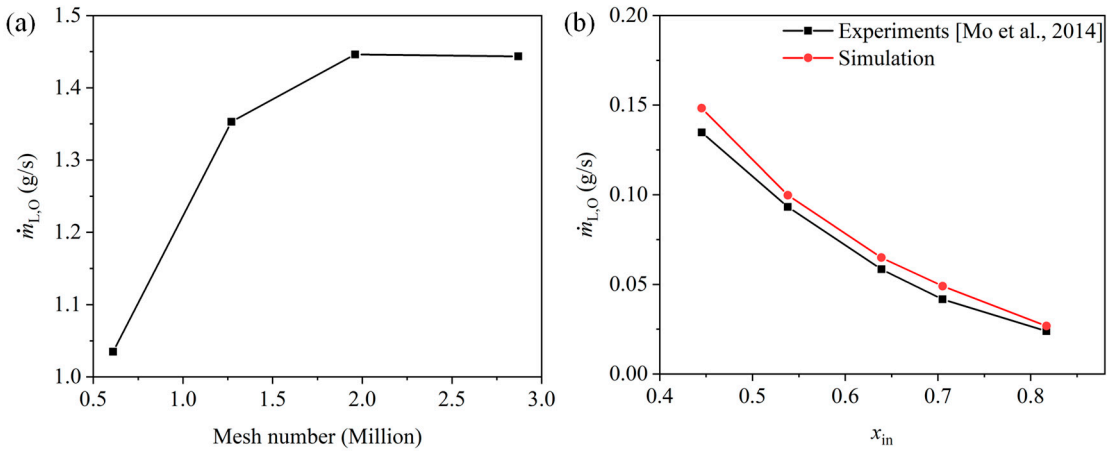

Figure 3. (**a**) Mesh-sensitive test; (**b**) model validation [15].

The numerical model is also validated based on the experiments [15]. It is seen from Figure 3b that when the inlet vapor quality x_{in} changes from 0.45 to 0.82, the average deviation between simulation data and experimental results is less than 10%, indicating good validity.

2.4. Evaluation Indicator

To evaluate the vapor-liquid separation performance, the vapor-liquid separation efficiency (η) is proposed (Equation (10)). It consists of two parts: the liquid drainage ratio (F_L) and the vapor leakage ratio (F_V). F_L is defined as the ratio of the liquid drainage from the orifice to the inlet, as shown in Equation (11). Similarly, F_V is defined as Equation (12).

$$\eta = |F_L - F_V| \tag{10}$$

$$F_L = \frac{\dot{m}_{L,O}}{\dot{m}_{L,in}} \tag{11}$$

$$F_V = \frac{\dot{m}_{V,O}}{\dot{m}_{V,in}} \tag{12}$$

3. Results and Discussion

In this paper, the two-phase flow characteristics in the branch outlets and orifices are comprehensively studied. The vapor-liquid separation performance and the phase distributions in the orifice are firstly investigated to obtain the vapor-liquid separation features. Then, the phase maldistributions in the branch outlet are discussed. Finally, the mechanistic model based on the force balance is established with a concern on the "droplet entrainment".

R134a is used as the working fluid and its properties are calculated by REFPROP [19]. The inlet operating conditions including temperature and vapor quality (x_{in}) are 45 °C and 0.5, respectively. To investigate its features under various conditions, the inlet mass flow rate ($\dot{m}_{in}$) is set in the range of 9–21 g/s based on scenarios in the air conditioning.

3.1. Performance of the Header and Flow Characteristics in the Orifices

The variation of η under different $\dot{m}_{in}$ is depicted in Figure 4. It can be observed that with the increasing of $\dot{m}_{in}$, η increases firstly to the maximum value of 51.94% at $\dot{m}_{in}$ = 12 g/s and then decreases. When $\dot{m}_{in}$ is larger than 15 g/s, the degradation of η becomes severer. It becomes 29.99% at $\dot{m}_{in}$ = 21 g/s. This will be discussed in the following section. The pressure difference (ΔP) crossing the orifice-baffle, which is one of the main driving forces for the liquid drainage [16], increases with the increasing of $\dot{m}_{in}$. This is because more liquid flows towards the right side of the orifice-baffle, leading to an increase in the height of the liquid film above the orifice-baffle. Thereafter, the static pressure above the orifice-baffle increases.

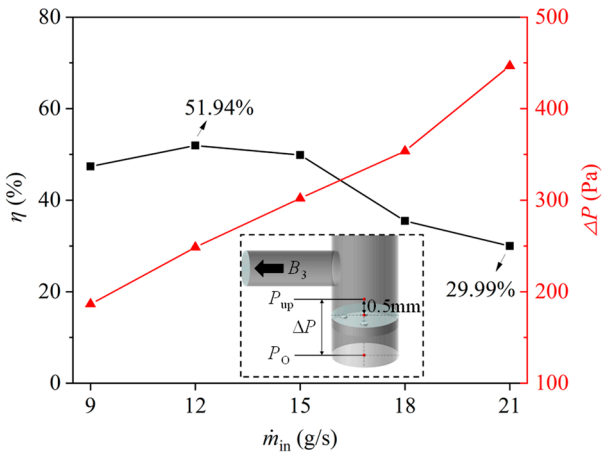

Figure 4. Vapor-liquid separation efficiency and the pressure difference across the orifice-baffle.

To obtain a deep understanding of the flow characteristic and discover the causes of deteriorated vapor-liquid separation performance, the mass flow rates of the liquid drainage and vapor leakage through the orifices, i.e., $\dot{m}_{L,O}$ and $\dot{m}_{V,O}$, are analyzed, as shown in Figure 5. As mentioned above, there exists a strong liquid impact at the right

side of the baffle, O_2, being the furthest away from the liquid impact, has a higher $\dot{m}_{L,O}$ than O_1 and O_3. Different from η that is peaked at $\dot{m}_{in}$ = 12 g/s, the peak of $\dot{m}_{L,O}$ = 3.75 g/s appears at $\dot{m}_{in}$ = 15 g/s. This is explained as: compared to $\dot{m}_{in}$ = 12 g/s, $\dot{m}_{in}$ = 15 g/s has a higher $\dot{m}_{L,O}$ because of a larger driving force, but its F_L is much smaller owing to the more liquid within $\dot{m}_{in}$, leading to a lower η given that F_V in these two cases are negligible (see Figure 5b). $\dot{m}_{L,O}$ maintains at around 3.30 g/s when $\dot{m}_{in}$ is 18 g/s and 21 g/s. Meanwhile, $\dot{m}_{V,O}$ weakens the vapor-liquid separation performance, derived from Equations (11) and (12). As seen in Figure 5b, $\dot{m}_{V,O}$ has an opposite trend to $\dot{m}_{L,O}$. It decreases at first when $\dot{m}_{in}$ is smaller than 15 g/s and then increases to 0.15 g/s at $\dot{m}_{in}$ = 21 g/s. The vapor only leakage about 0.02 g/s and 0.01 g/s as $\dot{m}_{in}$ equals to 12 g/s and 15 g/s, respectively. This is due to the liquid film above the orifice-baffle in these two cases being able to resist the impact of the liquid flow from the wall, in which the orifices are rarely affected by the fluid impact and only a small amount of vapor leakage. Conversely, much vapor leakage out from the orifice under the other three $\dot{m}_{in}$ because of the unstable liquid film above the orifice-baffle. Moreover, the vapor is escaped out from O_2 is less than that from O_1 and O_3 owing to its farthest distance away from the liquid impact.

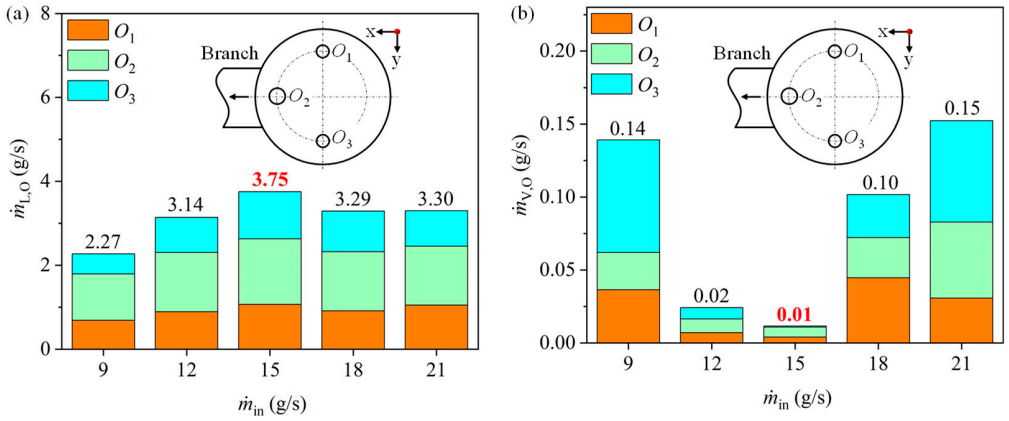

Figure 5. Mass flow rate of (**a**) liquid; (**b**) vapor at each orifice.

Figure 6 displays the distributions of vector and density at the central section of the orifices. Clearly, the flow characteristics in O_2 are significantly different from those in O_1 and O_3. When $\dot{m}_{in}$ is between 9–15 g/s, the vapor velocity in O_2 is normally lower than 1.5 m/s and it mostly exists near the wall of the orifice. As $\dot{m}_{in}$ increases, the vapor with high velocity begins to appear in O_2, which indicates more vapor leakage. This phenomenon is mainly due to the induced stronger liquid impact on the orifice-baffle at higher $\dot{m}_{in}$. As a result, the liquid film above the orifice-baffle is unable to resist the liquid impact and meanwhile the interactions between the liquid and vapor becomes intensive, leading to the increasing of $\dot{m}_{V,O}$. As for O_1 and O_3 that are closer to the liquid impact region, they are more likely to have a higher vapor velocity. As shown in Figure 6b, the velocity of the vapor in O_1 and O_3 can be up to 3 m/s as $\dot{m}_{in}$ = 9 g/s. However, with more liquid accumulated on the orifice-baffle (Figure 6c,d), the effect of the fluid impact on these two orifices weakens, with only a little vapor leakage out from the orifices. Further increasing $\dot{m}_{in}$ (Figure 6e,f), the liquid impact is enhanced again, contributing to a higher vapor velocity in O_1 and O_3. Summarily, the effects of the liquid impact on the orifice are the competitions between the liquid film on the orifice-baffle and $\dot{m}_{in}$. At the lower $\dot{m}_{in}$, the liquid film is too thin to resist the liquid impact and, consequently, the vapor escapes from the orifices, whereas at the higher $\dot{m}_{in}$, the interactions of the liquid and vapor are upgraded and the vapor is carried to the orifices by the liquid.

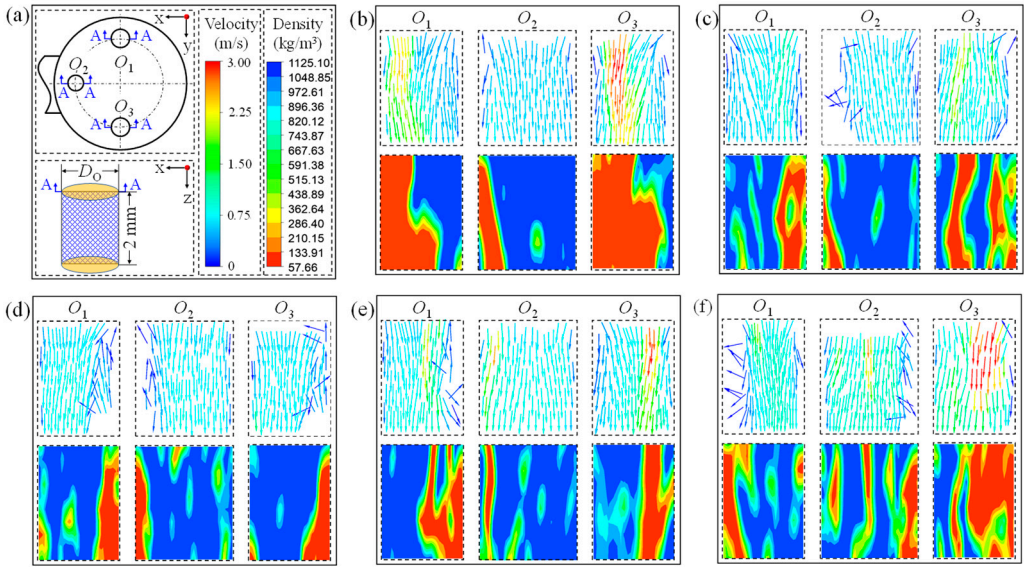

Figure 6. (**a**) Instructions and distributions of velocity and density in each orifice at (**b**) 9 g/s, (**c**) 12 g/s, (**d**) 15 g/s, (**e**) 18 g/s and (**f**) 21 g/s.

3.2. Flow Characteristics in the Branch Outlet

As shown in Figure 7, the maldistributions of $\dot{m}_B$ and x_B in the branch outlets are rather significant. The liquid mass flow rate in each branch outlet ($\dot{m}_{L,B}$) increases with the increasing of $\dot{m}_{in}$. Moreover, the liquid flows into the header and jets on the header wall of the header. A part of the liquid breaks up into droplets that are thereafter dragged into the branch outlets by the vapor, which is termed as "droplet entrainment". A similar phenomenon was also found by Li [12] and Zheng [20]. Obviously, $\dot{m}_{L,B}$ in B_3 is remarkably higher than that in B_1 and B_2. This is because the liquid flows to B_3 is not only by droplet entrainment, but also comes from the overflowing liquid from the orifice-baffle that cannot be drained promptly. However, the vapor in the branch outlet is more uniform than liquid owing to its lower inertia force. $\dot{m}_{V,B}$ in B_1 is slightly lower than B_2 and B_3 for the considered $\dot{m}_{in}$.

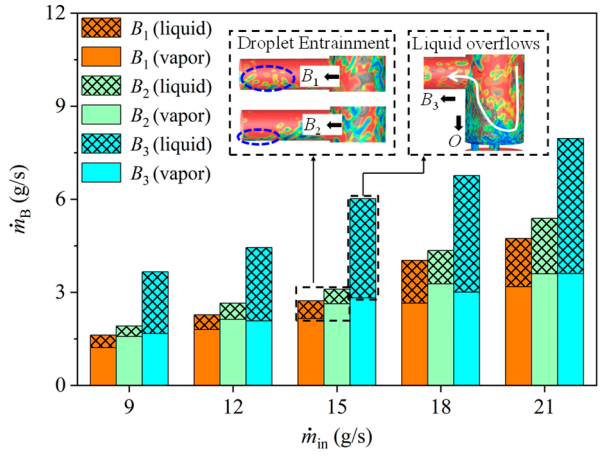

Figure 7. Mass flow rate in each branch outlet.

The droplets which enter the branch outlet is mostly due to the drag of the vapor. Hence, the vapor velocity is essential. To further explore the vapor flow characteristic, the vapor velocity distribution along each branch outlet and the specific header planes are plotted in Figure 8. The two-phase fluid flows from the branch inlet I_4 and mixes in S_{10}. Due to the inertia, the fluid gathers on the right side of the header and a vortex is generated on the left side, resulting in the vapor velocity on the left side being lower than that on the

right side. After S_{10}, the fluid continues to flow downwardly, and then a part of it is divided into the B_1 because of the suction of the branch outlet. The fluid is more accumulated at the lower part of B_1 due to the inertia (S_7), in which the vortex exists above the B_1 and shows a vapor velocity non-uniform distribution. The other part of the fluid from I_4 that cannot enter B_1 in time will keep flowing in the header. In this way, the fluid also flows on the left side, resulting in a lower non-uniformity at S_{11}. Similarly, the vapor velocity distribution in the next branch outlet (S_8) and header (S_{12}) are close to the S_7 and S_{11} respectively. However, due to the diversion of the fluid, the vapor velocity decreases correspondingly. On the other hand, in the B_3, the distribution of the vapor velocity is more uniform. This is mainly due to the fact that B_3 has a maximum mass flow rate than B_1 and B_2, in which case the fluid can be fully fill at the B_3, where there is no vortex generated. With the increase in $\dot{m}_{in}$, not only does the velocity increase but it also improves the non-uniformity of the velocity distributions.

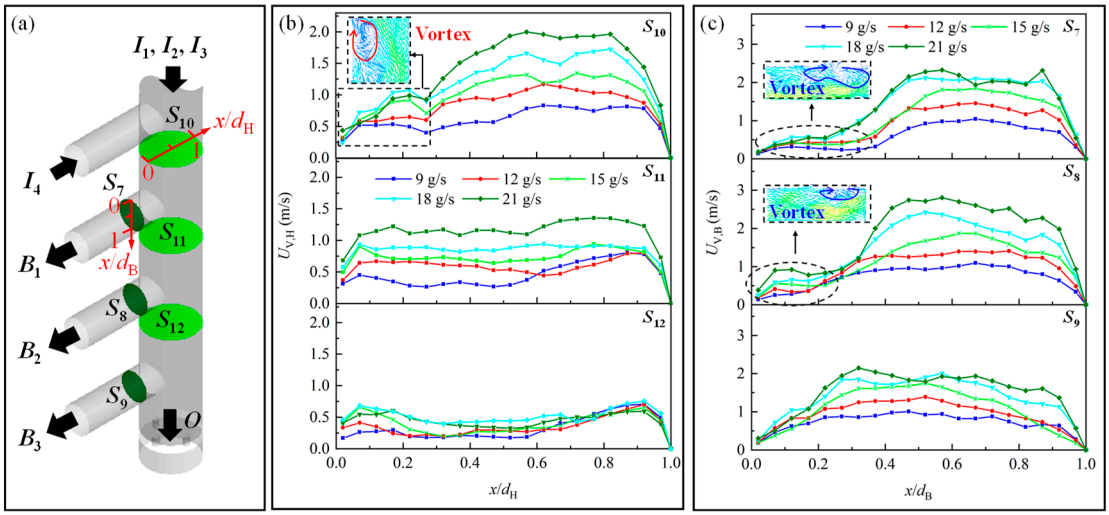

Figure 8. (**a**) Instructions and the vapor velocity distribution in (**b**) header and (**c**) branch outlet.

3.3. Mechanism Model of Droplet

As described above, the droplets in the branch outlets are dragged by the vapor. Meanwhile there exist vortexes in the header and the branch outlets, resulting in the mainstream area being smaller than the actual cross-section area, which substantially increases the local mass flux. According to the droplet model proposed by Tan [21] that is listed in Appendix A, the droplet diameter (d) is mainly affected by the mass flux that is relevant to the vortexes. Hence, the vortex has a great influence on the droplet entrainments. However, the vortexes are sometimes neglected when analyzing droplet [13]. In order to reveal the effect of the vortex on droplet characteristics, the force on the droplets is analyzed. Moveover, a critical vapor velocity for "droplet entrainment" ($U_{V,C}$) is also proposed. The following assumptions are made for the droplets: (1) they are spherical; (2) they have the same diameter in the same branch outlet.

Taking B_1 as an example, Figure 9 demonstrates d in the header and the vapor velocity in B_1 with and without vortex. It is observed that an increase in $\dot{m}_{in}$ leads to an enlarged droplet diameter and decreased vapor velocity simultaneously. In addition, the existence of the vortex decreases the droplet diameter by up to 1.76 times and increases the vapor velocity in the branch outlet by 35.10%, which significantly affects the forces of the droplet.

The force balance of the droplet is further established and analyzed. The droplet in the header is generally subjected to four forces (Figure 10), they are the gravitation force (F_G), the drag force (F_{D2}) and the buoyancy force (F_B) in the vertical direction as well as the drag force (F_{D1}) in the axial direction. The details of these four forces are described in Appendix B. In these four forces, F_G and F_B are only dominated by d. Moreover d, the

drag force (F_{D1} and F_{D2}) is also depended on the velocity. The higher mass flux represents the smaller droplet diameter. The drag force under different $\dot{m}_{in}$ is a result of the vapor velocity competing with d. As shown in Figure 11, the sum of forces in the vertical direction shows fluctuation with the increasing of $\dot{m}_{in}$ and the minimum value is 2.04×10^{-4} N at $\dot{m}_{in}$ = 12 g/s, while the force in the axial increases monotonously. F_{D1} and F_{D2} increases with the increasing of $\dot{m}_{in}$, which indicates the increasing rate of the velocity is larger than the decreasing rate of d. Meanwhile, F_G and F_B both decrease due to the droplet being smaller when increasing of $\dot{m}_{in}$. F_G at $\dot{m}_{in}$ = 21 g/s is only 1.02% to that at $\dot{m}_{in}$ = 12 g/s. Since F_G and F_B are only related to the density difference, F_G is constantly 20.14 times higher than F_B, which represents that in general, the force in the vertical upward is relatively small compared to the downward. Interestingly, the dominant force in the vertical direction switches from F_G to F_{D2} when $\dot{m}_{in}$ is higher than 12 g/s.

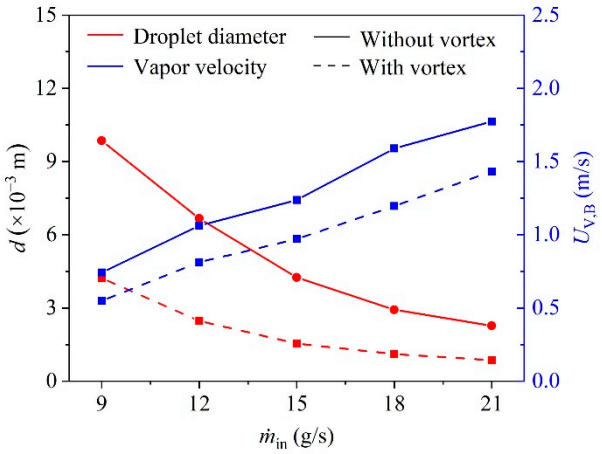

Figure 9. Droplet diameter and the vapor velocity in the branch outlet under various $\dot{m}_{in}$.

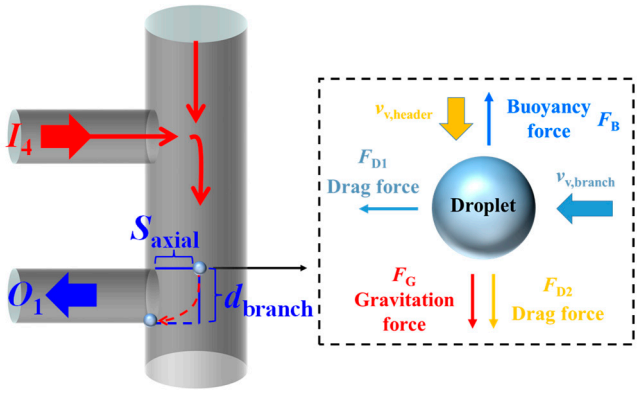

Figure 10. Forces on droplet in the header.

When the droplets flow into the intersection of the header and the branch outlet, the axial distance for droplets to be entrained to the branch outlet is S_{axial} and the vertical distance is the diameter of the branch outlet (d_B), as shown in Figure 10. If the flowing time of droplet in the vertical direction $t_{vertical}$ is longer than that in the axial direction t_{axial}, the droplet will be entrained to the branch outlet. Therefore, the critical point for the droplet entrainment is defined at $t_{vertical} = t_{axial}$. In this way, the critical vapor velocity ($U_{V,C}$) required to entrain the droplet can be obtained when the droplet in the branch outlets is located in S_{axial}, as calculated as in Equations (13)–(15).

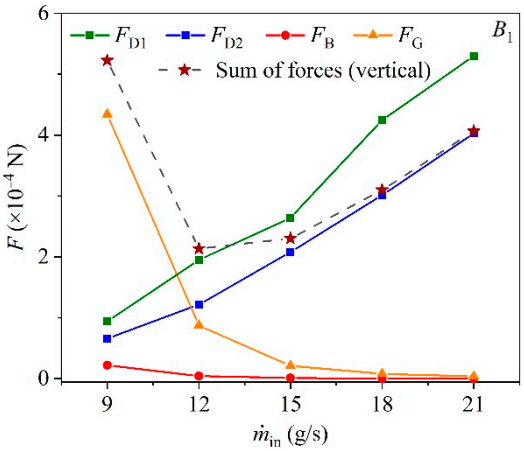

Figure 11. Forces on droplet under various $\dot{m}_{in}$.

$$U_{V,C} = \frac{8\rho_L d}{3C_d\rho_V {t_{vertical}}^2} {S_{axial}}^{0.5} \tag{13}$$

$$t_{vertical} = \left[\left(d_B + \frac{U_{L.H}^2}{2a_{vertical}} \right)^{0.5} - \frac{U_{L.H}}{(2a_{vertical})^{0.5}} \right] \left(\frac{2}{a_{vertical}} \right)^{0.5} \tag{14}$$

$$a_{vertical} = \frac{3C_d\rho_V}{4\rho_L d}(U_{V,H} - U_{L,H})^2 + \frac{g(\rho_L - \rho_V)}{\rho_L} \tag{15}$$

It can be observed that $U_{V,C}$ is highly correlated to the velocity of both phases in the header, the vapor velocity in the branch and d $U_{V,C}$ at the different axial locations under various $\dot{m}_{in}$ is plotted in Figure 12. Clearly, the larger S_{axial} requires a higher $U_{V,C}$ to entrain the droplet and the growth rate of the $U_{V,C}$ decreases as the S_{axial} increases. Moreover, under the same axial location, for the droplet to be dragged to the branch outlet needs a higher $U_{V,C}$ when $\dot{m}_{in}$ is increased. This is mainly due to the smaller d at higher $\dot{m}_{in}$, causing the larger acceleration and the shorter flow time $t_{vertical}$ in the vertical direction.

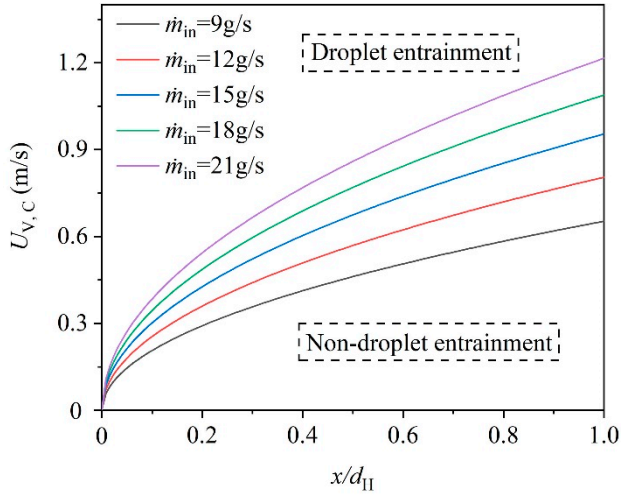

Figure 12. The critical vapor velocity with and without vortex under various $\dot{m}_{in}$.

It is worth mentioning that in this study, the velocity in the header and the branch outlets are simplified to be averaged from each plane. The distributions of the droplet are assumed to be uniform in the header. Nevertheless, for the actual flow, the distributions of velocity and the volume fraction are non-uniform and extremely complex. In future work,

the distribution characteristics of these parameters are of great interest to be quantified by a refined the model to improve the model accuracy.

4. Conclusions

Based on the VOF model and k-ε turbulence model, the flow characteristic of the fluid in the orifice-baffle header at various inlet operating conditions is simulated by CFD with attentions to the vortexes and droplets. Under the considered conditions, the conclusions are addressed as follows:

(1) The vapor-liquid separation efficiency maintains superior at the inlet mass flow rate of 9–15 g/s and then deteriorated as beyond 15 g/s. The maximum η are 51.94% at the inlet mass flow rate of 12 g/s;
(2) The liquid impact on the orifice-baffle results in the vapor leakage from the orifice. It becomes more intensive and is the main reason that deteriorates the separation performance when the inlet mass flow rate is higher than 15 g/s;
(3) The liquid maldistribution in the branch outlets is mainly because of the overflowing in B_3 that can be up to 4.36 g/s at the inlet mass flow rate of 21 g/s, whereas the vapor is more uniform distribution in the branch outlets owing to its lower inertia;
(4) The vortex in the header causes a decrease in the droplet diameter and an increase in the vapor velocity significantly in the branch outlet. The dominant force of the droplet in the vertical direction changes from F_G to F_{D2} as $\dot{m}_{in}$ increases.

Author Contributions: Conceptualization, J.C.; methodology, K.H.; software, K.H.; visualization, K.H. and Z.Y.; formal analysis, X.L.; investigation, J.C.; data curation, K.H.; writing—original draft preparation, K.H.; writing—review and editing, Y.L. and J.H.; supervision, J.C.; project administration, J.C.; funding acquisition, Y.C. All authors have read and agreed to the published version of the manuscript.

Funding: This research was funded by the National Natural Science Foundation of China (51736005), Guangdong Basic and Applied Basic Research Foundation (2022A1515012035) and Innovation Leadership of Sciences and Technologies Program in Guangdong Special Support Plan (2017TX04N371).

Institutional Review Board Statement: Not applicable.

Informed Consent Statement: Not applicable.

Data Availability Statement: Not applicable.

Conflicts of Interest: The authors declare no conflict of interest.

Nomenclature

Symbol	
$a_{vertical}$	Acceleration in the vertical direction, m/s^2
C_d	Drag force coefficient
$C_{1\varepsilon}$	Empirical constants, 1.42
$C_{2\varepsilon}$	Empirical constants, 1.68
C_μ	Empirical constants, 0.0845
d	Diameter, mm
F	Drainage (leakage) rate ratio
F_B	Buoyancy force, N
F_{D1}	Drag force (axial), N
F_{D2}	Drag force (vertical), N
F_G	Gravitational force, N
f	The friction factor of the vapor
G_k	Generation of turbulent kinetic energy
g	Gravitational acceleration, m/s^2
$\dot{m}$	Mass flow rate, kg/s
ΔP	Pressure difference, Pa
Re	Reynold number

S_{axial}	Axial distance, m
t	Time, s
$t_{vertical}$	Droplet flow time in the vertical direction, s
t_{axial}	Droplet flow time in the axial direction, s
U	Velocity, m/s
Greek Symbol	
α	Volume fraction
ε	Turbulence kinetic dissipation, m^2/s^3
η	Vapor-liquid separation efficiency
μ	Dynamic viscosity, $kg/(m^2 \cdot s^2)$
μ_t	Turbulence kinetic viscosity, $kg/(m^2 \cdot s^2)$
ρ	Density, kg/m^3
σ	Surface tension coefficient N/m
σ_k	Empirical constants, 1.0
σ_ε	Empirical constants, 1.2
Subscript	
B	Branch outlet
C	Critical
H	Header
in	Inlet
L	Liquid
O	Orifice outlet
S	Supercritical
V	Vapor

Appendix A

The droplet diameter is calculated based on Tan et al. [21], as shown in Equations (A1)–(A4).

$$d = \frac{8\sigma U_{L,S}}{f\rho_V U_{V,S}^3} \tag{A1}$$

$$f = \left[1.14 - 2\lg\left(\frac{21.25}{Re^{0.9}}\right)\right]^{-2} \tag{A2}$$

$$U_{L,S} = \frac{\dot{m}_{L,in}}{0.25\pi d_H^2} \tag{A3}$$

$$U_{V,S} = \frac{\dot{m}_{V,in}}{0.25\pi d_H^2} \tag{A4}$$

where the σ, $U_{L,S}$, $U_{V,S}$, ρ_V, f represents the surface tension surface tension, the supercritical velocity of liquid, the supercritical velocity of vapor, vapor density and the friction factor of the vapor.

Appendix B

The droplet in the header is generally subjected to drag force in the axial direction (F_{D1}), the gravitation force (F_G), the buoyancy force (F_B) and the drag force in the vertical direction (F_{D2}). They are evaluated as follow:

$$F_B = \frac{4}{3}\pi\left(\frac{d}{2}\right)^3 \rho_V g \tag{A5}$$

$$F_G = \frac{4}{3}\pi\left(\frac{d}{2}\right)^3 \rho_L g \tag{A6}$$

$$F_{D2} = \frac{1}{8}\pi d^2 C_d \rho_V (U_{V,H} - U_{L,H})^2 \tag{A7}$$

$$F_{D1} = \frac{1}{8}\pi d^2 C_d \rho_V U_{V,B} \quad \text{(A8)}$$

where $U_{V,H}$, $U_{L,H}$ and $U_{V,B}$ represent the vapor velocity and the droplet velocity in the header and the vapor velocity in the branch outlet, respectively. d is the droplet diameter. C_d is the drag force coefficient for the droplet, which is calculated by the classical model proposed by Schiller and Naumann [22], as shown in Equation (A9).

$$C_d = \begin{cases} \frac{24(1+0.15Re^{0.687})}{Re} & Re \leq 1000 \\ 0.44 & Re > 1000 \end{cases} \quad \text{(A9)}$$

References

1. Peng, X.; Wu, D.; Lu, G.; Wang, Z.; Huang, M. Liquid-Vapor Separation Air Condenser. China Patent No. 200610113304.4, 22 September 2006.
2. Li, J.; Yang, Z.; Hu, S.; Yang, F.; Duan, Y. Thermo-Economic Performance Improvement of Butane/Isopentane Mixtures in Organic Rankine Cycles by Liquid-Separated Condensation Method. *Appl. Therm. Eng.* **2020**, *181*, 115941. [CrossRef]
3. Hua, N.; Xi, H.; Xu, R.J.; Chen, Y.; Wang, H.S. Numerical Simulation of Multi-Pass Parallel Flow Condensers with Liquid-Vapor Separation. *Int. J. Heat Mass Transf.* **2019**, *142*, 118469. [CrossRef]
4. Zhong, T.M.; Chen, Y.; Zheng, W.X.; Hua, N.; Luo, X.L.; Yang, Q.C.; Mo, S.P.; Jia, L.S. Experimental Investigation on Microchannel Condensers with and without Liquid-Vapor Separation Headers. *Appl. Therm. Eng.* **2014**, *73*, 1510–1518. [CrossRef]
5. Zhong, T.; Chen, Y.; Hua, N.; Zheng, W.; Luo, X.; Mo, S. In-Tube Performance Evaluation of an Air-Cooled Condenser with Liquid-Vapor Separator. *Appl. Energy* **2014**, *136*, 968–978. [CrossRef]
6. Li, J.; Hrnjak, P. Improvement of Condenser Performance by Phase Separation Confirmed Experimentally and by Modeling. *Int. J. Refrig.* **2017**, *78*, 60–69. [CrossRef]
7. Chen, J.; Ding, R.; Li, Y.; Lin, X.; Chen, Y.; Luo, X.; Yang, Z. Application of a Vapor–Liquid Separation Heat Exchanger to the Air Conditioning System at Cooling and Heating Modes. *Int. J. Refrig.* **2019**, *100*, 27–36. [CrossRef]
8. Li, Y.; Chen, J.; Lin, X.; Yang, Z.; Chen, Y.; Luo, X. Quantification on the Effects of Liquid-Vapor Separation in Air-Conditioning System by Using Advanced Exergy Analysis. *J. Therm. Sci.* **2020**, *29*, 597–608. [CrossRef]
9. Chen, J.; Chen, L.; Lin, X.; Chen, Y.; Luo, X.; Yang, Z.; Liang, Y. Performance of Heat Pump Water Heater (HPWH) with and without Liquid-Separation: Detailed Experimental Comparisons. *Appl. Therm. Eng.* **2020**, *179*, 115713. [CrossRef]
10. Lu, P.; Luo, X.; Wang, J.; Chen, J.; Liang, Y.; Yang, Z.; Wang, C.; Chen, Y. Thermo-Economic Design, Optimization, and Evaluation of a Novel Zeotropic ORC with Mixture Composition Adjustment during Operation. *Energy Convers. Manag.* **2021**, *230*, 113771. [CrossRef]
11. Oh, K.; Lee, S.; Park, T.; Kim, Y. Multistage Gas and Liquid Phase Separation Condenser. U.S. Patent 10/444,486, 23 May 2003.
12. Li, J.; Hrnjak, P. Visualization and Quantification of Separation of Liquid-Vapor Two-Phase Flow in a Vertical Header at Low Inlet Quality. *Int. J. Refrig.* **2018**, *85*, 144–156. [CrossRef]
13. Li, J.; Hrnjak, P. Parametric Study and Improvement of Phase Separation in Intermediate Headers of Microchannel Condensers. *J. Fluids Eng. Trans. ASME* **2020**, *142*, 2–12. [CrossRef]
14. Li, J.; Hrnjak, P. Numerical Study of R134a Liquid-Vapor Flow in a Vertical Header for Phase Separation with Low Inlet Quality. *Int. J. Refrig.* **2021**, *129*, 11–21. [CrossRef]
15. Mo, S.; Chen, X.; Chen, Y.; Yang, Z. Passive Control of Gas-Liquid Flow in a Separator Unit Using an Apertured Baffle in a Parallel-Flow Condenser. *Exp. Therm. Fluid Sci.* **2014**, *53*, 127–135. [CrossRef]
16. Li, Y.; Luo, X.; Wang, Z.; Yang, Z.; Chen, J.; Liang, Y.; Wang, C.; Chen, Y. Numerical Simulation on the Header-Orifice Structure-Based Liquid-Vapor Separator Used in Liquid-Separation Condenser. *Chem. Eng. Sci.* **2021**, *235*, 116475. [CrossRef]
17. Chen, J.; Li, Y.; Ding, R.; Lin, X.; Chen, Y.; Luo, X.; Yang, Z. Comparative Performance of Air-Conditioning Systems with Different Refrigerant Circuitries in Liquid-Separation Condenser. *Int. J. Refrig.* **2018**, *92*, 154–164. [CrossRef]
18. El Hajal, J.; Thome, J.R. Condensation in Horizontal Tubes, Part 1: Two-Phase Flow Pattern Map. *Int. J. Heat Mass Transf.* **2003**, *46*, 3349–3363. [CrossRef]
19. Lemmon, E.W.; Huber, M.L.; McLinden, M.O. *NIST Standard Reference Database 23: Reference Fluid Thermodynamic and Transport Properties-REFPROP*; Version 10; National Institute of Standards and Technology: Gaithersburg, MD, USA, 2018.
20. Su, W.; Hwang, Y.; Deng, S.; Zheng, N.; Zhao, L.; Lu, P. Experimental Study on Phase Separation of Refrigerant at Horizontal T-Junction. *Int. J. Multiph. Flow* **2018**, *105*, 217–233. [CrossRef]
21. Tan, X.H.; Li, X.P.; Liu, J.Y. Model of Continuous Liquid Removal from Gas Wells by Droplet Diameter Estimation. *J. Nat. Gas Sci. Eng.* **2013**, *15*, 8–13. [CrossRef]
22. Schiller, L.; Naumann, Z. A Drag Coefficient Correlation. *Z. Ver. Deutsch. Ing.* **1935**, *77*, 318–320.